RESEARCH ARTICLE
10.1029/2023SW003749

Key Points:

- Statistics of M-I coupling in a coupled geospace model are analyzed and validated with empirical models and observations
- The comparisons for different interplanetary magnetic field orientations and Kp indices suggest the updated M-I model produces reasonable average patterns
- The updated model exhibits a significantly improved M-I current-voltage relation compared with previous model results

Correspondence to:
J. Chen,
cjjvince@hku.hk

Validation of Simulated Statistical Characteristics of Magnetosphere-Ionosphere Coupling in Global Geospace Simulations Over an Entire Carrington Rotation

Qianfeng Yin[1], **Kevin H. Pham[2]**, **Junjie Chen[1]**, and **Binzheng Zhang[1]**

[1]NWU-HKU Joint Center of Earth and Planetary Sciences, Department of Earth Sciences, the University of Hong Kong, Pokfulam, China, [2]High Altitude Observatory, National Center for Atmospheric Research, Boulder, CO, USA

Abstract We study the statistical features of magnetosphere-ionosphere (M-I) coupling using a two-way M-I model, the GT configuration of the Multiscale Atmosphere Geospace Environment (MAGE) model. The M-I coupling characteristics, such as field-aligned current, polar cap potential, ionospheric Joule heating, and downward Alfvénic Poynting flux, are binned according to the interplanetary magnetic field clock angles over an entire Carrington Rotation event between 20 March and 16 April 2008. The MAGE model simulates similar distributions of field-aligned currents compared to empirical Weimer/AMPS models and Iridium observations and reproduces the Region 0 current system. The simulated convection potential agrees well with the Weimer empirical model and displays consistent two-cell patterns with SuperDARN observations, which benefit from more extensive data sets. The Joule heating structure in MAGE is generally consistent with both empirical Cosgrove and Weimer models. Moreover, our model reproduces Joule heating enhancements in the cusp region, as presented in the Cosgrove model and observations. The distribution of the simulated Alfvénic Poynting flux is consistent with that observed by the FAST satellite in the dispersive Alfvén wave regime. These M-I coupling characteristics are also binned by the Kp indices, indicating that the Kp dependence of these patterns in the M-I model is more effective than the empirical models within the Carrington Rotation. Furthermore, the MAGE simulation exhibits an improved M-I current-voltage relation that closely resembles the Weimer model, suggesting that the updated global model is significantly improved in terms of M-I coupling.

Plain Language Summary Geospace, the region of space surrounding Earth, encompasses the magnetosphere-ionosphere (M-I) system and is strongly influenced by the solar wind. The interaction between the magnetosphere and ionosphere, known as M-I coupling, is crucial for understanding and forecasting space weather. In this study, we use an updated global physics-based model of the coupled M-I system to simulate various M-I parameters, including field-aligned current, polar cap potential, ionospheric Joule heating, and downward Alfvénic Poynting flux, and their responses to different upstream solar wind conditions over an entire 28-day Carrington Rotation event. The statistical analysis of our simulation is validated by comparing it with observations and empirical models. The comparisons for different interplanetary magnetic field orientations and Kp indices suggest the updated M-I model produces reasonable average patterns and demonstrates significant improvements in M-I coupling characteristics. Our study provides valuable insights into the dynamics of M-I coupling and improves our ability to predict and mitigate the impact of space weather events on our technology.

1. Introduction

The study of the magnetosphere-ionosphere (M-I) coupling has been a major focus of research in the field of geospace for several decades (Goertz & Boswell, 1979) due to its importance in space weather forecasting. As magnetospheric currents flow into and out of the conductive polar ionosphere along equipotential magnetic field lines, a coupled M-I current system is formed. In this process, the associated ionospheric polar electric fields enable high-latitude plasma convection and induce heating through the collision between ions and neutral gases, known as Joule heating. Additionally, energetic charged particles precipitate into the upper atmosphere in the auroral region along the Earth's magnetic field lines, ionizing thermospheric neutrals and causing heating/up-welling of the thermosphere (Bjoland et al., 2015; Codrescu et al., 1995; Wang et al., 2020). These processes are driven by the interaction between the solar wind (SW) and the Earth's magnetosphere, largely dependent on the orientation of the interplanetary magnetic field (IMF) (Wang et al., 2004). By accurately forecasting space weather, we can more effectively mitigate the impact of space weather events on our technological infrastructure.

To achieve accurate space weather forecasting, it is crucial to have a deep understanding of M-I coupling dynamics. To address this, researchers have developed various methods, including empirical models and global physical simulations. Empirical models, such as the Weimer 05 model (Weimer, 2005), offer a convenient and efficient proxy for observations under many circumstances. This model utilizes data collected by the Dynamics Explorer 2 satellite, which operated in a polar orbit at altitudes of 300–1,000 km between August 1981 and March 1983. Another example is the Average Magnetic field and Polar current System (AMPS) empirical model (Laundal et al., 2018), which characterizes the average ionospheric magnetic field and current system for specific solar wind speed, IMF vector, orientation of the Earth's magnetic dipole axis, and solar flux index ($F_{10.7}$). Derived from measurements, this model utilizes data sets from the Challenging Minisatellite Payload (CHAMP) and Swarm satellites in low Earth orbit (Laundal et al., 2018). However, since these models rely on historical data, they may underestimate system variations during more pronounced changes. The limitations of empirical models emphasize the significance of physics-based global model simulations, which provide a more comprehensive understanding of M-I coupling dynamics and can better predict space weather events. Global simulations have been increasingly employed to study M-I coupling under various SW/IMF conditions. These models, grounded in physical principles, provide a deeper understanding of the underlying phenomena. For instance, the Lyon-Fedder-Mobarry (LFM) model is a three-dimensional, time-dependent, ideal MHD code that solves the equations of MHD in a spherical coordinate system with a constant ionospheric conductance function as the inner boundary. The model can simulate the global structure and dynamics of the magnetosphere and its interaction with the solar wind and the ionosphere (Lyon et al., 2004). The Open Geospace General Circulation Model (OpenGGCM) is a global model designed to simulate the magnetosphere-ionosphere system. It operates by solving the MHD equations in the outer magnetosphere. Through field-aligned current (FAC), electric potential, and electron precipitation, it couples with an ionosphere potential solver and the Coupled Thermosphere-Ionosphere Model (CTIM) that is a coupling of the LFM model with a global physics-based ionosphere model Thermosphere-Ionosphere-Electrodynamics General Circulation Model (TIEGCM). It can capture the feedback effects between the magnetosphere and ionosphere/thermosphere, such as the ionospheric outflow, the thermospheric heating and cooling, and the ion-neutral drag (Wang et al., 2004; Wiltberger et al., 2004). By doing so, OpenGGCM offers a comprehensive, global perspective of the magnetosphere-ionosphere system (Raeder et al., 2008). The Block-Adaptive Tree Solarwind Roe-type Upwind Scheme (BATS-R-US), similar to LFM and OpenGGCM, is an MHD model designed for studying the global magnetosphere and its coupling with the ionosphere. Unlike fixed grid models, BATS-R-US utilizes a block-adaptive mesh, offering flexibility with Cartesian or generalized coordinates, including spherical, cylindrical, and even toroidal grids. While block-adaptive grids are commonly used in astrophysics and aerospace engineering, their implementation in BATS-R-US enhances its versatility and suitability for modeling complex phenomena in the Earth's magnetosphere-ionosphere system (Tóth et al., 2012). In addition, other geospace IT models or frameworks, such as the Space Weather Modeling Framework (SWMF) (Tóth et al., 2005) and Coupled Thermosphere Ionosphere Plasmasphere Electrodynamics (CTIPe) model (Codrescu et al., 2012) have also been developed in the past decades.

By comparing simulation results with observations and empirical models, researchers can evaluate their performance and refine the models for increased accuracy. For instance, Huang et al. (2006) compared LFM simulation results with an empirical model and observations to investigate the magnetic field configuration and plasma distribution in the inner magnetosphere, discussed approaches for improving the LFM model. Guild et al. (2008a) conducted a statistical validation effort, comparing the central plasma sheet properties from 6-year Geotail observations with 2-month LFM simulations to systematically evaluate the performance of the global MHD model. Similarly, Zhang et al. (2011) analyzed long-term M-I coupling characteristics, such as FAC, polar cap potential, downward Poynting flux, and vorticity of ionospheric convection, by comparing LFM simulations with observed statistical averages and the Weimer 05 empirical model results. Wiltberger et al. (2017) utilized the LFM global MHD models with three different resolutions and the Weimer (2005) empirical model to examine the structure of the high-latitude FAC patterns. Wang et al. (2004) compared the simulation results from the CMIT model with the Thermosphere–Ionosphere Nested Grid (TING) empirical model, founding that the CMIT model predicted higher cross polar cap potential drops and more enhanced neutral temperatures and winds than the empirical model. Zhang et al. (2019) developed an improved global MHD model, the Grid Agnostic MHD for Research Applications (GAMERA), by inheriting the core numerical philosophy of the LFM model and combining many algorithmic and computational improvements. TIEGCM has also been developed into a high-horizontal resolution version (1.25° × 1.25 and 0.625° × 0.625°) in geographic longitude–latitude coordinates

through a ring average technique (Dang et al., 2021). The recent development of the coupled M-I model has enabled studies for complex interactions between the Earth's magnetosphere and ionosphere-thermosphere (Lin et al., 2021; Pham et al., 2022), providing valuable insights into and space physics research and space weather prediction. The Multiscale Atmosphere Geospace Environment (MAGE) model couples the global magnetosphere MHD code, GAMERA (Zhang et al., 2019), with the global ionosphere-thermosphere code, TIEGCM (Richmond et al., 1992; Roble et al., 1988). Pham et al. (2022) used MAGE to simulate consecutive neutral density changes observed by satellites during a geomagnetic storm, which offers a deeper understanding of the observed phenomenon, and compared the results with a standalone ionosphere-thermosphere simulation driven by an empirical model of high latitude electrodynamics.

The enhanced physics-based simulation models play a pivotal role in investigating the characteristics of M-I coupling. The comparison of physics-based simulations with empirical models or observational data provides valuable benefits in improving simulation models and establishing an effective global framework for point measurements. However, it is important to consider that the average statistical results may significantly differ from the instantaneous results (Zhang et al., 2012). Therefore, rigorous statistical analyses must be conducted by comparing large, long-period data sets of observed and simulated parameters to assess the model's capability to replicate and forecast the global climatological processes (Guild et al., 2008a, 2008b). Classifying the data sets of main parameters by IMF clock angle is a conventional statistical method. However, classification according to the Kp index can be also used as a supplement in the research of testing model applicability and exploring other aspects, which has not been explored in prior simulations, largely due to the fact that most simulation models are unable to reproduce the process with the situation under high Kp values (Kp > 4).

In this study, we use an improved global geospace model to simulate the M-I coupling system under observed IMF/SW conditions within an entire Carrington Rotation. Our focus is on investigating the statistical features of various parameters, including FAC, ionospheric convection pattern, Joule heating, and Alfvénic Poynting flux, which are classified by both IMF clock angle and Kp index. To validate our simulation results for M-I coupling, we have compared them with data sets of various observations, including Iridium, SuperDARN, FAST, and Polar satellite, and empirical models such as Weimer 05 and AMPS. Furthermore, we compare the simulated current-voltage relationships with the previous global MHD model, that is, LFM model, and Weimer 05 empirical model. In Section 2, we describe the coupled global geospace model and the simulation setup. In Section 3, we illustrate the statistical results of M-I coupling parameters such as FAC, convection pattern, and Joule heating and select some results for comparison with observations and empirical models. Finally, we summarize our findings in Section 4.

2. Model and Method

2.1. The Coupled M-I Model

The developed global model of coupled M-I system, the MAGE model (Lin et al., 2021; Pham et al., 2022), includes magnetosphere MHD code, GAMERA (Zhang et al., 2019) and global ionosphere-thermosphere code, TIEGCM (Richmond et al., 1992; Roble et al., 1988). These two codes are coupled by exchanging parameters across their interfaces through an M-I coupler module, the RE-developed Magnetosphere-Ionosphere Coupler/Solver (REMIX) (Merkin & Lyon, 2010). The REMIX module determines the electric fields at the inner boundary of GAMERA based on the polar conductance from the TIEGCM code, while it specifies the high-latitude connection and auroral electron precipitation in the TIEGCM code based on the current and plasma moments from the GAMERA code. The time step of exchanging information is 5 s. We note that we use the "GT" configuration of the MAGE model only couples GAMERA and TIEGCM, and does not include the Rice Convection Model (RCM) (Toffoletto et al., 2003). At present, including RCM in a long duration simulation is detrimental to the coupled results. The loss rate in RCM is calculated via a "fudge" factor of 1/3 where the loss rate is always set to 1/3 regardless of the surrounding conditions. In addition, the refilling rate in the current implementation of RCM is simplistic. Furthermore, in a single fluid MHD approximation, the cold RCM plasmaspheric fluid becomes mixed with the hotter MHD GAMERA fluid, creating a lukewarm but dense fluid. For a long duration run, all three issues are compounded, resulting in a significantly more unrealistic magnetosphere. Therefore, results presented in this study use the GT configuration of MAGE without RCM. We use the same version of the code as those found in Pham et al. (2022) and refer to the simulation results as the GT simulation. Further details about the M-I coupling can be found in Pham et al. (2022).
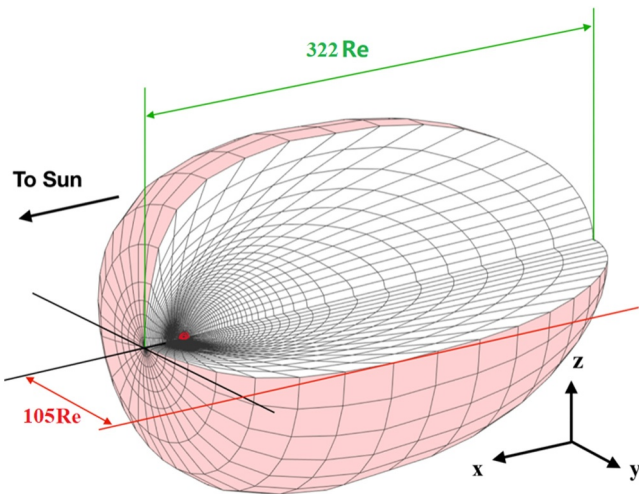
Figure 1. Grid exhibition with $32 \times 24 \times 32$ cells, corresponding approximately to spherical (radial × meridional × azimuthal) coordinates. This study uses $96 \times 96 \times 128$ resolution. The outer boundary takes the shape of an egg with its symmetry axis aligned along the SM X-axis, the inner boundary positioned at 2 R_E, the Earth locates at the center of the red region.

The GAMERA module for the magnetosphere is a newly developed MHD code that combines geometric flexibility with high-order spatial reconstruction and constrained transport to maintain a divergence-free magnetic field, inheriting the legacy of the LFM global MHD code (Lyon et al., 2004). It has algorithms and software improvements on the use of flexible grid specifications, grid metric calculations based on high-order Gaussian quadrature, seventh-order upwind spatial reconstruction, nonclipping flux limiters, and a higher-order conservative averaging-reconstruction method for axis singularity and hybrid MPI-OMP parallelization (Zhang et al., 2019). These improvements allow for easier application to multidimensional MHD flow simulations in non-orthogonal curvilinear grids adapted to specific conditions and more efficient large-scale simulations of the MHD problem. The GAMERA model simulates the interactions between the solar wind and Earth's magnetosphere by solving ideal MHD equations on a non-orthogonal curvilinear grid (Sorathia et al., 2020; Zhang et al., 2017, 2019). In the solar-magnetospheric (SM) coordinates, the magnetospheric simulation domain extends from 28 Earth radii (R_E) sunward to - 294 R_E anti-sunward and spans approximately 105 R_E in directions perpendicular to the Earth-Sun axis. In this simulation, we use a medium resolution of the code, with $96 \times 96 \times 128$ cells in the radial, meridional, and azimuthal directions (Shown in Figure 1), corresponding to an about $1° \times 1°$ resolution in magnetic latitude (MLAT) and longitude at ionospheric reference altitude of 100 km. The measurements are taken along the geomagnetic field lines from the inner boundary of GAMERA (2 R_E) to the ionosphere. The computational grid is adapted to be nonuniform to achieve higher resolution near the magnetosheath, in the plasma sheet and inner magnetosphere, with lower resolution far away from the earth in the solar wind and at the outer boundaries of the simulation. The MHD calculation of the magnetospheric plasma stops at a spherical surface at a geocentric radial distance of 2 R_E, which is also defined as the low-altitude (inner) boundary of the global simulation. The electric field inputs at the inner boundary are specified by the TIEGCM code and REMIX module. The methodology for calculating precipitation is described in Zhang et al. (2015), where they devised a model for lower energy, broadband, and direct-entry cusp precipitation, based on the general techniques utilized in LFM (Wiltberger et al., 2009).

The TIEGCM module solves time-dependent equations of momentum, energy, and continuity for the neutrals and ions of the coupled global ionosphere-thermosphere system (Richmond et al., 1992; Roble et al., 1988). To adapt the resolution to match the GAMERA module, this study uses a high horizontal resolution of $1.25° \times 1.25°$ in geographic latitude-longitude grids, which was developed by Dang et al. (2021). The polar inputs are from the magnetosphere. The solar EUV radiation is driven by $F_{10.7}$ solar index. The lower boundary is influenced by the diurnal and semi-diurnal migrating tides, which are specified by the Global Scale Wave Model (Hagan & Forbes, 2002, 2003). The polar inputs of high-latitude connection and auroral electron precipitation from the magnetosphere are provided by the GAMERA code and REMIX module. The code calculates ionospheric conductance by integrating the effects of solar ionization and energetic particle precipitation from the magnetosphere. These effects are modulated by the impact parameter and the density of ionized particles. The Pedersen conductivity (S/m) is expressed as:

$$\sigma_P = \frac{q_e}{B}\left[N_{O^+}\frac{\gamma_{O^+}}{1+\gamma_{O^+}^2} + N_{O_2^+}\frac{\gamma_{O_2^+}}{1+\gamma_{O_2^+}^2} + N_{NO^+}\frac{\gamma_{NO^+}}{1+\gamma_{NO^+}^2} + N_e\frac{\gamma_e}{1+\gamma_e^2} \right] \tag{1}$$

The Hall conductivity (S/m) is:

$$\sigma_H = \frac{q_e}{B}\left[-N_{O^+}\frac{1}{1+\gamma_{O^+}^2} - N_{O_2^+}\frac{1}{1+\gamma_{O_2^+}^2} - N_{NO^+}\frac{1}{1+\gamma_{NO^+}^2} + N_e\frac{1}{1+\gamma_e^2} \right] \tag{2}$$
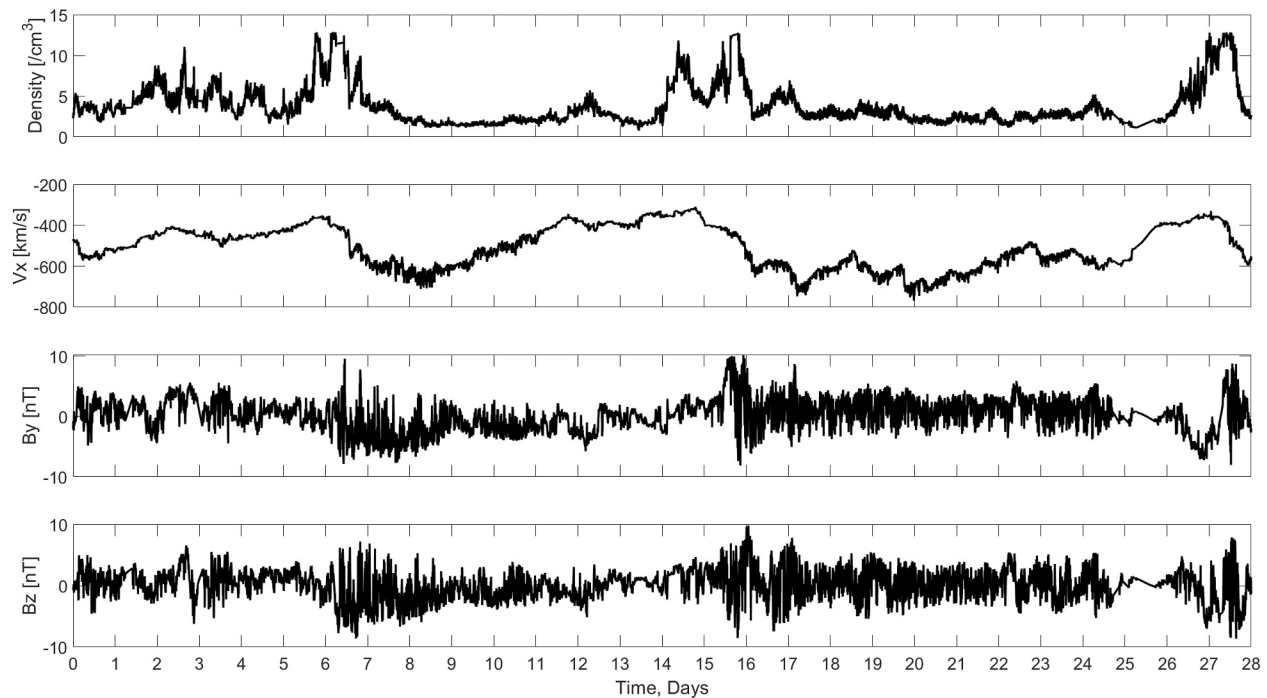
Figure 2. SW/IMF data used in the Carrington Rotation event simulation. From the top to the bottom panels are solar wind velocity, density, IMF By and B_z components, respectively.

where the q_e is the electron charge, B denotes the magnetic field, N_i and γ_i represents the number densities in $1/cm^3$ and the ratios between collision frequency and gyro frequency for components "i," such as ions O^+, O_2^+, NO^+, and electron e.

2.2. The 20 March–16 April 2008 Event

The simulation in this study is during an entire Carrington Rotation event from 20 March 2008 to 16 April 2008. The Carrington Rotation event was selected for this study because it has a broad range of solar wind driving conditions, with the SW number density ranging from 0.8 to 12.9 cm^{-3}, and the IMF B_z varying from −9 to 10 nT, among other parameters. During this period, the selected Carrington Rotation event was relatively quiet, with Kp indices ≤5 and Dst indices >−55 nT, indicating a lack of extreme values typically associated with major geomagnetic storms. The observed period corresponded to a solar minimum (Figure S1 in Supporting Information S1). This allowed for the study of the general characteristics of M-I coupling, unaffected by intensive solar activity such as solar flares and coronal mass ejections (CMEs). Since the selected Carrington Rotation event was near March equinox, the average dipole tilt angle during this period is small and the M-I statistics in the northern and southern hemispheres are similar, only the simulation data from the northern hemisphere are analyzed. A subset of the upstream SW/IMF observations during the Carrington Rotation event extracted from the OMNI data set via the CDAWeb (https://cdaweb.gsfc.nasa.gov/) are shown in Figure 2, the data selected in this study has a strong continuity including variations of the solar wind speed, number density, IMF B_y and B_z components. There are occasional data gaps in this study resulting from limitations in observation techniques. These gaps were addressed through interpolation methods, either linearly or non-linearly, depending on the physical properties of the parameters. However, such occurrences are infrequent, and their impact on the analysis is minimal.

Note that the M-I coupling characteristics simulated by the GT simulation will be compared with the LFM results during another Carrington period (Zhang et al., 2011). However, the similar statistical behaviors of the inner and outer boundary conditions in each IMF orientation between these two periods, such as $F_{10.7}$ and IMF-Bz (Figures 1 and 2), indicate that the difference between these two periods does not affect the conclusion regarding the comparison of GT and LFM results.
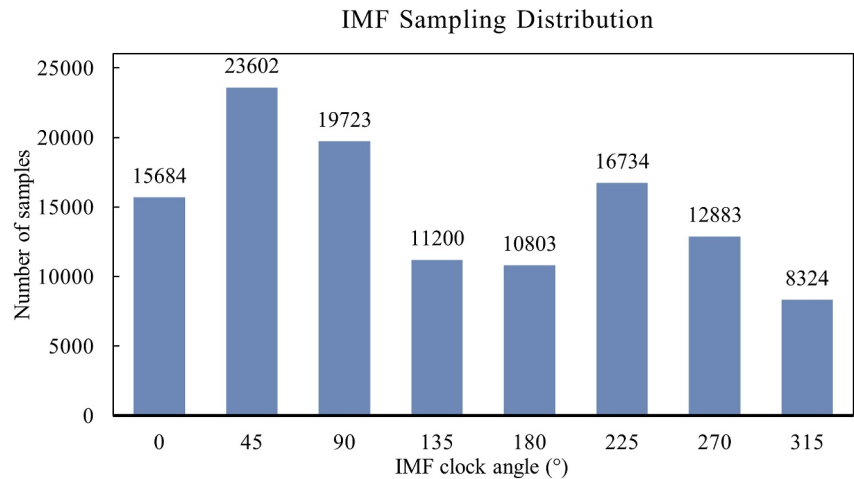
IMF Sampling Distribution

Figure 3. Number of simulation samples in each IMF clock angle bin. 0° means the northward IMF clock bin, 90° means the eastward, 180° means the southward, 270° means the westward.

To analyze the statistics of the M-I coupling characteristics of the simulation, the data is first grouped by the IMF clock angle, which is divided into eight 45-degree bins. Each bin covers a range of 45° centered at the labeled orientation shown in Figure 3 (0°, 45°, …, 315°). For example, the 0° clock angle (northward) bin includes all intervals with IMF orientations from −22.5° to 22.5°. The number of sample distributions in each IMF clock angle bin is shown in Figure 3. In this Figure, each IMF clock angle bin contains over 8,000 samples, providing a relatively large sample size for statistical representation of the M-I coupling in the code. When analyzing the correlation between the upstream driving conditions and the response of the M-I system, the results were delayed due to the propagation of SW/IMF from the upstream boundary (30 R_E sunward from the Earth) to the Earth. Therefore, the lag time of ionospheric response should be considered when analyzing the relationship between the IMF clock-angle distribution and the ionospheric results. Figure 4a shows samples of B_z and CPCP time series used in the cross-correlation analysis. We chose a constant average lag time based on a cross-correlation analysis between IMF B_z and the CPCP since the variation of the solar wind and IMF is slow. Figure 4b shows the cross-correlation function between B_z and CPCP. The cross-correlation function peaks at 14 min, which is chosen to be the average lag time in the following analysis of IMF clock-angle and Kp index dependences.

3. Results and Discussion

3.1. Statistical Classification of M-I Parameters by the IMF Orientation

Figure 5a shows the average distributions of the ionospheric FAC (positive downward) calculated from the GT simulation binned by IMF clock angle indicated in the center panel. The magnitudes of total inflow currents are labeled at the bottom right of each panel. The Region I (R1) currents, which occur between 70° and 80° MLAT, flow downward on the dawnside and upward on the duskside, whereas the direction of the Region II (R2) currents, which occur between 55° and 70° MLAT, show the opposite dawn-dusk dependence. Overall, the large-scale FAC distribution in the GT simulation is consistent with the typical R1 and R2 FAC systems observed in the Triad observations (Iijima & Potemra, 1976, 1978; Wiltberger et al., 2017).

The merging between the SW and the M-I system is highly dependent on the orientation of the IMF. Higher magnetic reconnection rates occur at the magnetopause when the IMF has a larger southward component, resulting in enhanced M-I coupling parameters, including the average ionospheric FAC, convective potential and Joule heating distribution. In Figure 5a, as the IMF clock angle turns from northward to southward, the magnitude of the currents is enhanced, with a hemispheric downward flowing current of approximately 1.8 MA, which is about 3.6 times greater than that of the hemispheric current in the northward IMF bin. Moreover, under the northward IMF clock angle conditions, a pair of FACs occurs at polar latitudes (above 80° MLAT), exhibiting opposite directions compared to the typical R1 currents. This polar FAC system, first identified by Iijima et al. (1984) and referred to as Region 0 (R0) currents or "NBZ" (northward B_z) Birkeland currents, is consistent with previous LFM simulation (Zhang et al., 2011), despite the limited modeling of the polar region in the latter
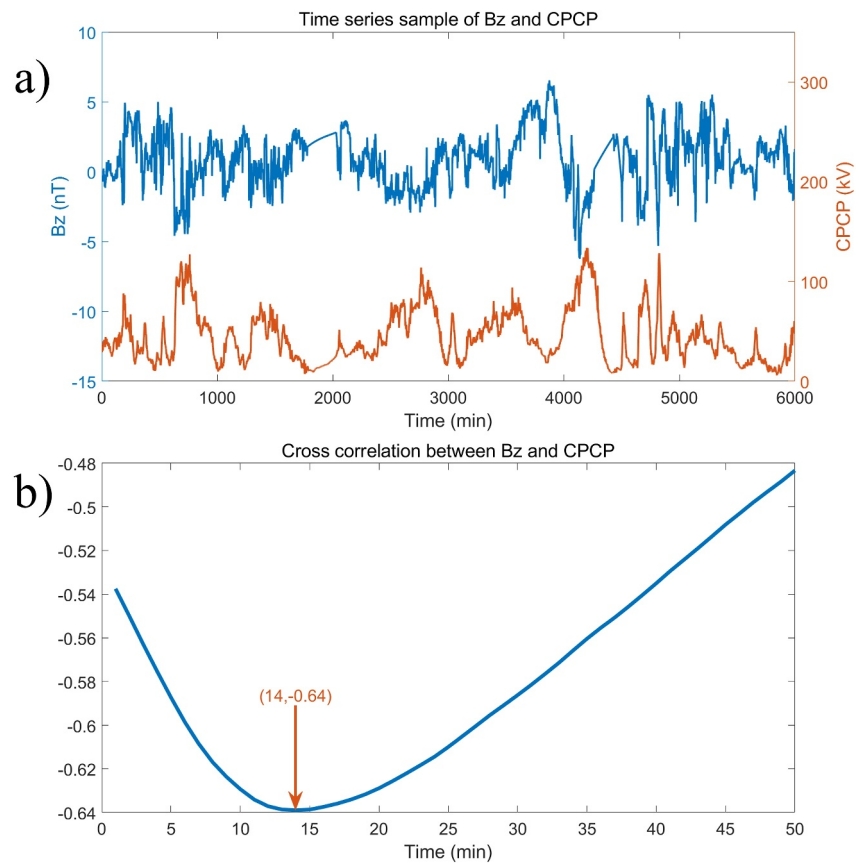
Figure 4. (a) The time series of B_z and CPCP for cross-correlation analysis. (b) The cross-correlation function for the selected B_z and CPCP series.

due to lower resolution. Owing to the improved grid resolution, the FAC system in the R1 and R2 regions is well-defined without numerical dispersion around the polar region in the GT simulation.

The statistical method used in the Weimer 05 empirical model is similar to that used in the physics-based global simulations. Results are calculated based on instantaneous SW/IMF conditions and then categorized according to the IMF clock angle. Figure 5b shows the IMF clock angle-dependent statistical distribution of ionospheric FAC derived from the empirical model. Compared to the simulation results (Figure 5a), the general patterns of FAC in the empirical model are similar under involving southward IMF conditions (Figure 5, the bottom 3 panels, middle panels on the left and right). Both exhibit typical R1 and R2 FAC patterns and a similar boundary shape between the R1 and R2 regions. However, the Weimer empirical model displays an intricate spiral nesting pattern in the polar region, which is not shown in the GT simulation and observations. Furthermore, the total downward (input) FAC in the GT simulation is approximately 10% smaller than that of the Weimer 05 empirical model in Figure 5b for the southeastward, southward and southwestward IMF bins (Figure 5b, the bottom 3 panels). Additionally, the R0 FAC system is not obviously separated from the R1 current.

In order to further validate the accuracy of our simulations, besides the Weimer empirical model, we also compare our simulation results with those obtained from another empirical model, the AMPS model. Figure 6 displays the statistical distribution of the FACs derived from the AMPS empirical model under the same average clock-angle binned IMF conditions as the GT simulation. The AMPS empirical is developed using the combined data sets of CHAMP and Swarm satellite observations (Laundal et al., 2018). The IMF clock angle dependence of the FAC morphology in the AMPS empirical model is similar to that in the GT simulation and the Weimer empirical model. It shows the R0 FAC system under the northward IMF clock angle bin and the typical R1/R2 FAC systems under the southward IMF. The GT simulation shows that the total downward current is about 15%–25% lower than those from AMPS for southeastward and southward IMF bins. Conversely, for other IMF clock angle
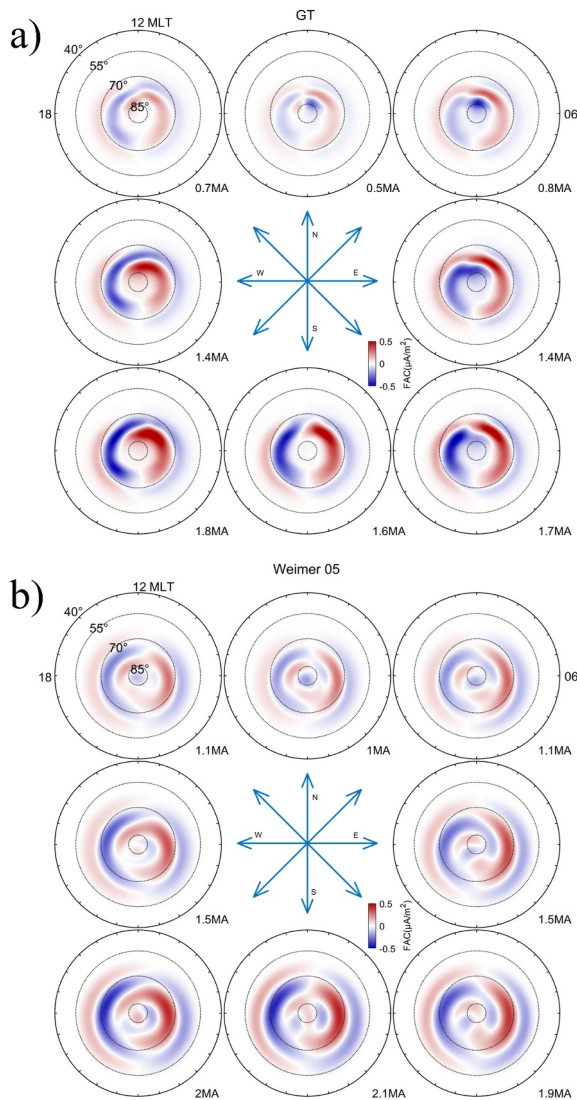
Figure 5. Statistical distributions of ionospheric FAC obtained from (a) the GT simulation and (b) the Weimer 05 empirical model under the same conditions for GT simulations. The SM axis N, E, S, and W correspond to northward, eastward, southward, and westward IMF at the subsolar dayside magnetopause, respectively.

conditions, the GT simulation shows a larger total downward current compared to AMPS. In terms of the spatial distribution of FAC, the GT simulation has a better agreement with the AMPS empirical model than with the Weimer 05 empirical model. The GT simulation exhibits higher 2D correlation coefficients with AMPS model under all IMF clock angle bins compared to those of Weimer 05, as illustrated in Figure 9.

Comparisons between observation and simulation results are also necessary to validate global simulations and advance the understanding of observations. Figure 6b in Zhang et al. (2011) showed the statistical distribution of IMF clock angles for the FAC systems, derived from a database of 1,550 Iridium observations at 2-hr intervals under stable IMF conditions (Anderson et al., 2008). The distribution of the average FAC system in our simulations (Figure 5a) is more consistent with the Iridium observations than the Weimer model predictions. Besides the R0 current pattern during the northward IMF conditions, our simulation also reproduces the pronounced upward current on the dawnside at high latitudes near the magnetic pole in the northeastward IMF bin, as shown in the top right panel in Figure 5a. This feature is observed in the Iridium data (Figure 6b in Zhang et al., 2011) and AMPS empirical model but not shown in the Weimer 05 empirical model (Figure 5b). The total downward currents in the GT simulation are generally similar to the Iridium results during most IMF orientation conditions, they differ by no more than 40%. This difference is likely due to the fact that the statistical Iridium samples were derived from a period with similar but not exactly the same driving conditions as those for our simulation.

Figure 7a shows the average convection patterns in the northern hemisphere derived from the GT simulation, binned according to IMF clock angles. The average CPCP values are labeled at the bottom right of each panel. A basic two-cell convection pattern is evident for clock angle bins with southward IMF (Figure 6a). As the IMF clock angle changes from northward to southward, the convection potential increases. The average CPCP reaches a minimum of 17 kV and a maximum of 82 kV for the northward and southwestward IMF clock angles, respectively. Moreover, the average CPCP values with the westward IMF are greater than those with the eastward IMF. The ionospheric electric potential exhibits typical crescent and round cell patterns, where the original two cells are distorted into crescent-shaped and round-shaped convection regions. Under eastward IMF conditions, a crescent-shaped convection cell is shown in the dawn region, while a round-shaped cell is shown in the dusk region. On the other hand, for westward IMF conditions, an opposite dawn-dusk asymmetric convection cell is shown (Tenfjord et al., 2015). However, this phenomenon is not as evident in previous LFM simulations, and the CPCP values in LFM simulations were 39% higher than those in GT simulations. The improvement in the GT simulation on the value and pattern of ionospheric electric potential may be related to the upgrade of the numerical algorithms dealing with the inner boundary conditions, although in Zhang et al. (2011) the high CPCP value was attributed to the lack of a drift-kinetic inner magnetosphere model. Further analysis is required to determine the exact cause of the difference in the CPCP values between the global models.

Figure 7b displays the ionospheric convection patterns predicted by the Weimer 05 empirical model, which are driven by the same SW/IMF conditions used in the GT simulation. Both the Weimer empirical model and the GT simulation depict similar two-cell convection patterns under all IMF clock angles. When the IMF clock angle is in the east-west direction, the patterns show a noticeable dawn-dusk asymmetry, with the positive crescent cell on the dawnside being further enhanced. Under southward IMF conditions (the bottom panels in Figure 7a), the CPCP values obtained from the GT simulation reach a peak of 82 kV, which is approximately 17% higher than the peak CPCP value of 70 kV predicted by the Weimer model. While driven by east-west IMF conditions (the middle two panels in Figure 7a), the CPCP values agree well with predictions from Weimer 05. Under northward IMF
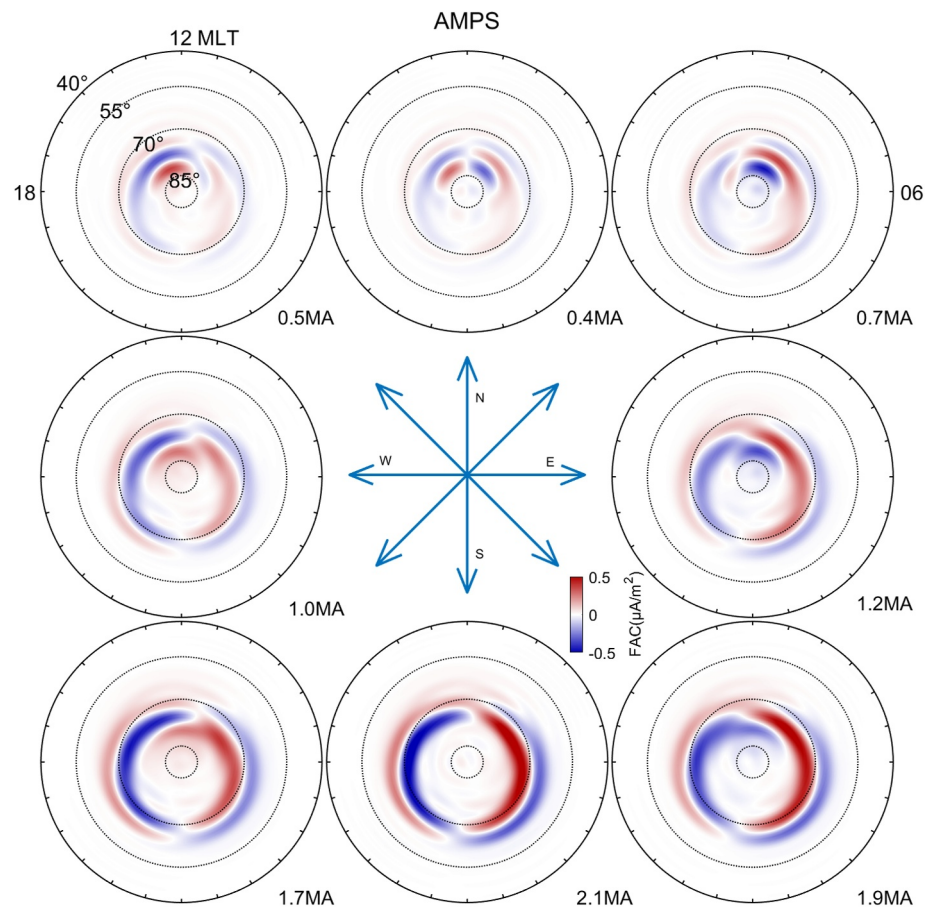
Figure 6. Statistical distributions of ionospheric FAC obtained from the AMPS empirical model.

conditions (the middle top panel in Figure 7a), the minimum CPCP value in the simulation is 17 kV, which is about 51% lower than the 35 kV from the Weimer results. Note that Weimer 05 has a built-in floor value corresponding to a $B = 0$ nT viscous potential during northward IMF (Bruntz et al., 2012). However, the GT simulation does not impose a specific lower limit on the CPCP, as it is determined by a combination of solar wind and ionospheric conditions. Consequently, during the Carrington Rotation where Weimer 05 reaches its floor value, the CPCP values of the GT simulation continue to decrease. This behavior is attributed to the significant reduction in potential values during northward IMF caused by the anti-sunward flows observed by Bhattarai et al. (2012).

We also compare the convection pattern derived from our GT simulations with the statistics derived from SuperDARN observations (Pettigrew et al., 2010). Figure 7c is captured from Zhang et al. (2011), which shows the observational convection patterns obtained from SuperDARN data of 5 years. The IMF conditions of the observation are binned by the same IMF clock angle as the simulation. The morphology of the convection pattern and the IMF clock angle dependence in our GT simulations are consistent with SuperDARN statistics. In fact, the convection pattern has been significantly improved in the GT simulation compared to the LFM simulation presented in Zhang et al. (2011). However, we note that the CPCP values of the simulation are greater than those of SuperDARN observations by a factor of about 1.3, especially for southward IMF conditions. We attribute this to two factors: first, the statistical processing of the SuperDARN data may introduce systematic underestimation of the CPCP, and second, the data sets selected from SuperDARN observations are the five years of 1998–2002 (inclusive) with $|B_z|$ between 3 and 5 nT, which is different from the Carrington Rotation event simulated in this study. Furthermore, there is a notable inconsistency between the input $F_{10.7}$ index utilized in the simulation during the Carrington Rotation and the values derived from SuperDARN observations spanning a period of 5 years.
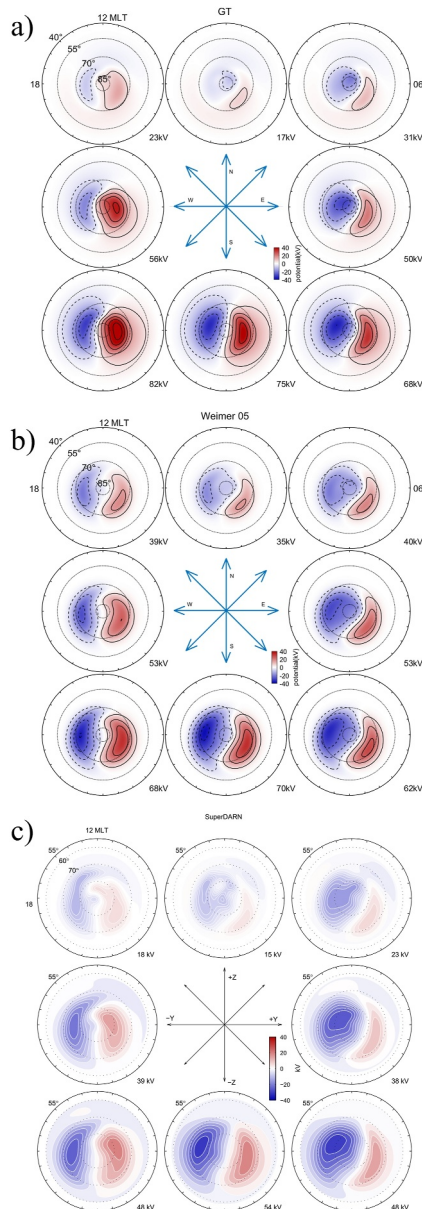
Figure 7. Statistical convection patterns obtained from (a) the GT simulation and (b) the Weimer 05 empirical model under the same IMF conditions as the GT simulation. (c) The observational convection patterns obtained from SuperDARN data of 5 years (Zhang et al., 2011).

Figure 8a presents statistical distributions of average Joule heating in the northern hemispheric obtained from the GT simulation, binned by IMF clock angles. The ionospheric Joule heating is crucial in understanding M-I coupling, as it describes the amount of electrodynamic energy transferred from the magnetosphere into the ionosphere-thermosphere system. The hemispheric integrated power corresponding to each clock angle bin is labeled in the bottom right corner. As the IMF orientation rotates from northward to southwestward, the total Joule heating increases by nearly eight times from a minimum of 11 GW to a maximum of 84 GW. The Joule heating is primarily distributed in the area between R1 and R2 current systems in Figure 5a, which are configured by the Pedersen conductivity. The closure of the R1 and R2 currents, through the Pedersen current, drives most of the electromagnetic heating in the ionosphere. It is important to note that the topology of Joule heating corresponds with the total horizontal sheet current densities in the Northern Hemisphere during the equinox, as presented by AMPS empirical model in Laundal et al. (2018). Our simulation is also conducted during this period. The average patterns of the ionospheric Joule heating indicate that the R1 currents are mostly close to the R2 currents at lower latitudes (around 70° MLAT) in the GT simulation, while a small portion is closed through the polar cap due to the lack of a drift-kinetic ring current model. This distribution of the ionospheric Joule heating is a significant improvement compared to the LFM long-run results presented in Figure 8c that is Figure 9a of Zhang et al. (2011), which is likely a consequence of improved grid resolution since neither study used a drift-kinetic ring current model.

Another significant improvement occurs in the polar cusp region, where the GT simulation results show a distinct enhancement of Joule heating rate. In the GT simulation, the cusp makes a dominant contribution to the overall energy budget, especially when the IMF clock angle ranges from the northeast to the west. Moreover, the heating rate is also significant when the IMF is southward. The simulation agrees well with the empirical model of the DC (direct current) Poynting flux developed by Cosgrove et al. (2014), which was derived from data obtained by the FAST satellite, and the observations (e.g., Billett et al., 2021; Li et al., 2011), but the cusp feature was missing in the previous LFM simulation (shown in Figure 8c). Moreover, the heating rate was dominant in the high latitude (above 75° MLAT) polar region (above 75° MLAT (Zhang et al., 2011), suggesting that the majority of the R1 currents in the LFM simulation close through the polar ionosphere. Figure 8b exhibits the corresponding distributions of average Joule heating rate predicted by the Weimer 05 empirical model. As shown in Figure 8b, the total Joule heating increases from 16 to 76 GW as the IMF clock angle rotates from north to south, by a factor of less than 5. Under southward IMF conditions, the statistical patterns of the GT simulation and the Weimer 05 empirical model exhibit enhanced Joule heating mostly between R1 and R2 currents without a significant cusp feature. The discrepancy between the Weimer 05 and the Cosgrove empirical model is out of the scope of our study, which is possibly due to the difference in the orbital coverage of different satellite data sets. For instance, the pressure fronts may only have temporal impacts which are not well captured by an average of satellite data obtained at widely spaced times and locations, as suggested by Weimer (2005).

Figure 9a illustrates the temporal variation of key M-I parameters (FAC, CPCP, Joule heating), derived from GT and Weimer 05 empirical model within the Carrington Rotation. The correlation coefficients for FAC, CPCP, and Joule heating are 0.7325, 0.7876, and 0.7934, respectively, although the Weimer 05 results show obvious built-in floor values (Bruntz et al., 2012). It is further shown that GT and Weimer 05 have a considerable degree of similarity. Figure 9b presents the 2D correlation coefficients of FAC between the GT and both the AMPS and
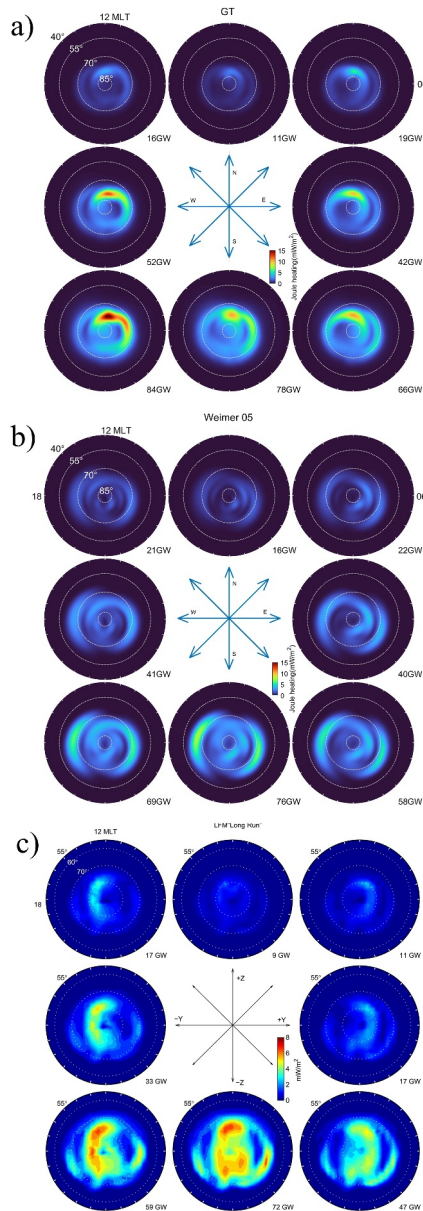
Figure 8. Statistical distributions of ionospheric Joule heating obtained from (a) the GT simulation, (b) the Weimer 05 empirical model, under the same conditions as the GT simulation, (c) LFM long run simulation.

Weimer 05 empirical models. It also shows the convection patterns and Joule heating between the GT and Weimer 05 empirical model. As previously discussed, the correlation of these key parameters between GT and either Weimer 05 or AMPS provides a quantitative measure of their similarity. It is noteworthy that the convection pattern similarity between GT and Weimer 05 is high, with numerous coefficients exceeding 0.9. This is particularly evident in the eastward (90°), southeastward (135°), southward (180°), and southwestward (225°) directions.

Figure 10 presents the distribution of average downward Alfvénic Poynting flux in the northern hemispheric ionosphere, derived from the GT simulation based on the band-passed filtering algorithm developed by Zhang et al. (2012). The bottom right corner shows the hemispheric integrated power corresponding to each clock angle bin. It is noteworthy to mention that Alfvén waves have a significant impact on the M-I coupling process, which is a significant component of geomagnetic storms and associated energy flow into the auroral acceleration region (Keiling et al., 2019). In the GT simulation, the Alfvénic Poynting flux $S_\parallel$ is calculated from perturbation electric (δE) and magnetic fields (δB) as:

$$S_\parallel = \frac{1}{\mu_0} \delta E \times \delta B \cdot \frac{B}{B}, \tag{3}$$

where μ_0 is the permeability of free space, and B is the mean vector magnetic field recorded at 1 R_E altitude, which is calculated from a 180-s running average. Perturbation δE and δB were calculated by subtracting a 180-s running average of each field from the instantaneous value of each step (15 s). The resulting Alfvénic Poynting flux values were then projected to a reference ionospheric altitude of 100 km by mapping $S_\parallel/B$ = constant along dipolar geomagnetic field lines.

The simulation reveals that when driven by northward IMF conditions (top three panels in Figure 10), the intensity of Alfvénic Poynting flux is low (0.6–0.7 GW) and mostly concentrated on the dayside, around 75° Latitude in the prenoon and postnoon sectors. The hemispheric integrated Alfvénic power peaches the lowest value of 0.6 GW under a purely northward IMF clock angle. The lack of intense nightside Alfvénic Poynting flux is a result of the fact that magnetotail activities were not enabled under northward IMF driving. However, the simulations performed using the LFM method, as reported by Zhang et al. (2014), did not show any apparent activity in the Alfvénic Poynting flux involving northward IMF clock angle bins. In fact, there was even zero total downward Alfvénic power under purely northward IMF conditions. T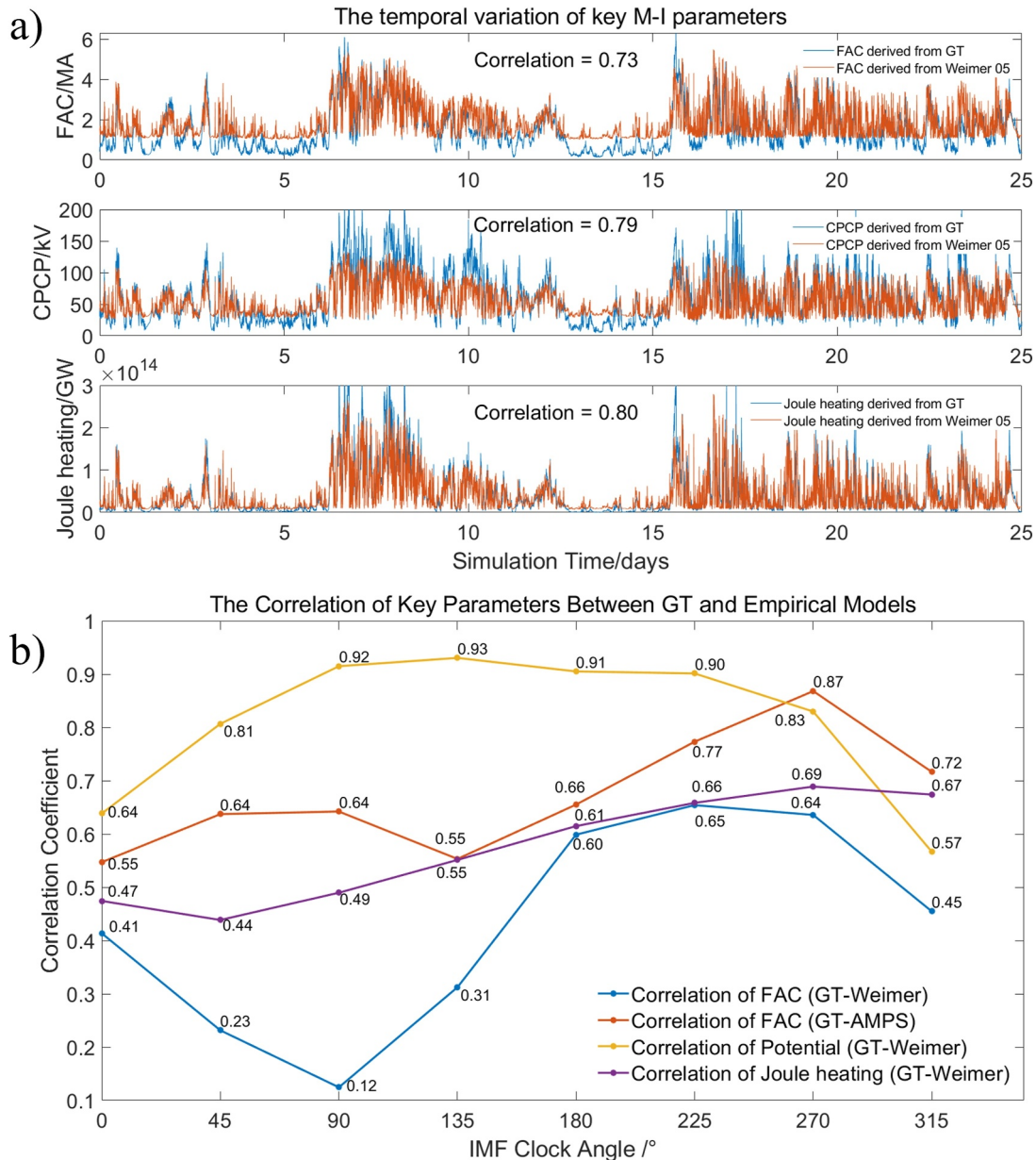his discrepancy is a consequence of using constant SW/ IMF conditions in the Zhang et al. (2014) simulations, while in this study the upstream conditions are changing in time, causing disturbances in the dayside magnetosphere. Under the westward-eastward IMF conditions (the left center and right center panels in Figure 10), the primary locus of enhanced Alfvénic Poynting flux activity on the dayside occurs around both 9:00 and 15:00 magnetic local times (MLTs). With the IMF rotating from north to south, the integrated power increases from 0.6 to 1.3 GW with a pronounced enhancement in the premidnight sector, which is caused by the meridional gradient of ionospheric Hall conductance (Lotko et al., 2014). These statistical characteristics are consistent with the distributions of inertial Alfvén wave (IAW) Poynting flux observed by FAST and shown in Figure 2a of Hatch et al. (2017). This simulated dawn-dusk asymmetry can be supported by many observations, such as the dawn-dusk asymmetry in the post-substorm period driven by southward IMF observed by the Polar satellite and SuperMAG ground magnetometer (Keiling et al., 2020).

Figure 9. (a) The temporal variation of key M-I parameters (FAC, CPCP, Joule heating), derived from GT and Weimer 05 empirical model. (b) The 2D correlation coefficients of key parameters between GT and empirical models.

3.2. Statistical Classification of M-I Parameters by the Kp Index

The geomagnetic Kp index is widely recognized as a significant indicator of geomagnetic activity and is utilized extensively within both scientific and operational communities. This index quantifies the disturbance in the Earth's magnetic field, which is brought on by the impact of the solar wind (Matzka et al., 2021). In this study, the maximum value of Kp, as determined during the Carrington Rotation, is established to be 5. To further highlight the characteristics of the M-I coupling, we have conducted a statistical classification of some key simulation parameters based on the Kp index. The objective of this classification is to provide an initial illustration of the variation of M-I coupling parameters under increasing Kp indices.

Figure 11a shows the simulated average FAC patterns in the northern hemisphere, binned by the Kp index during the Carrington Rotation. The total downward current is labeled on the bottom right of each panel. When the Kp index is less than 1, and the total downward current flowing into the ionosphere is 0.5 MA. As the Kp index
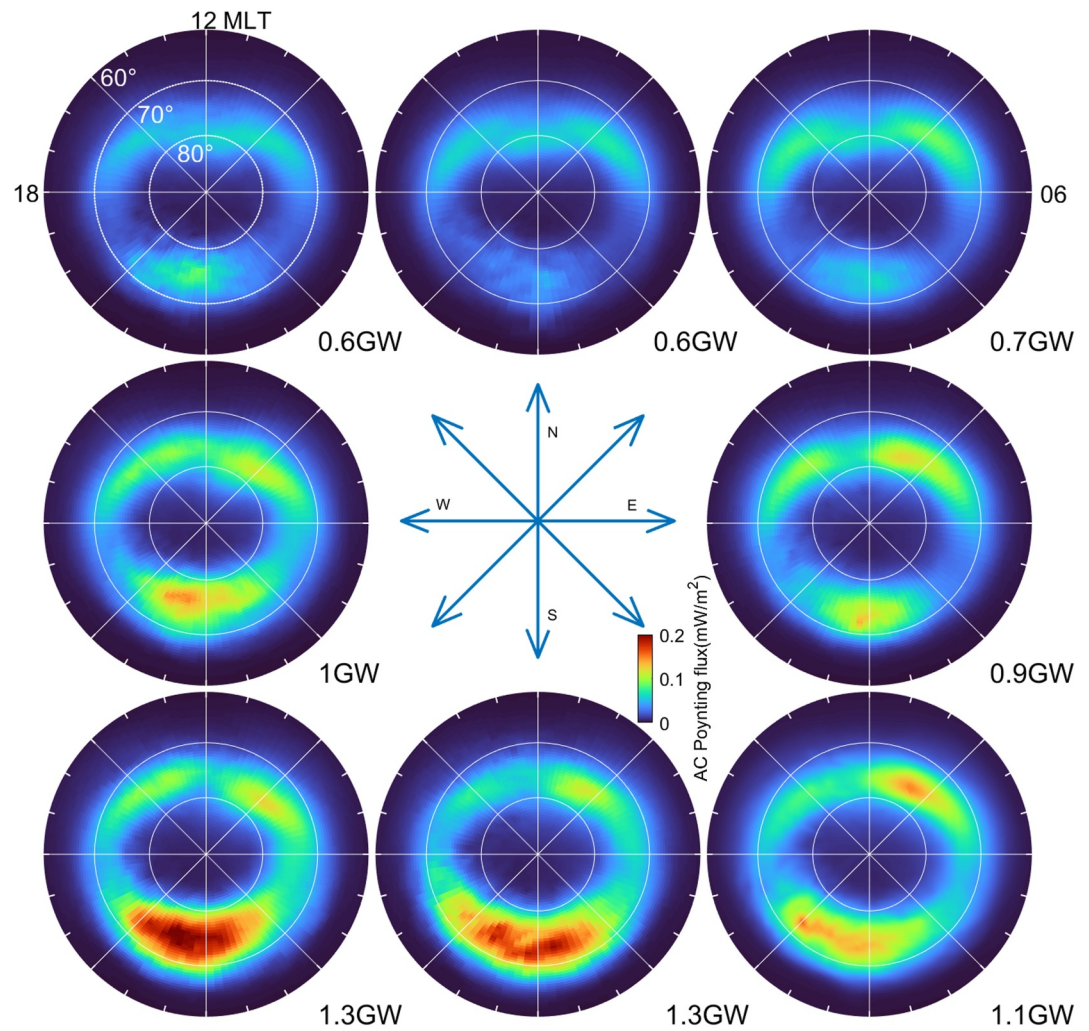
Figure 10. Statistical distributions of ionospheric Alfvénic Poynting flux obtained from the GT simulation.

increases, the total downward current increases from 0.5 to 2.5 MA, leading to a more pronounced pattern and topology similar to that shown in Figure 5a. For high Kp values, the pattern is more similar to GT results under a southwestward IMF clock angle. Figure 11b displays the FAC patterns, derived from Weimer 05 empirical model using the same statistical method and IMF conditions as the GT simulation throughout the Carrington Rotation. The variation of the GT simulation with increasing Kp index is consistent with the Weimer 05 empirical model results, with the total inward currents increasing from 1.1 to 2.7 MA and the R2 currents becoming more pronounced. However, for the Kp index ≤2, the total inward current in the empirical model is higher than that in the GT simulation. Moreover, due to the absence of RCM, the simulated values in R2 do not exhibit significant enhancement comparable to Weimer 05 for high Kp conditions. Additionally, the Weimer results display traces of a current system near the magnetic pole that are not evident in the GT simulations.

Figure 12a exhibits the statistical distributions of ionospheric convection patterns, classified by the Kp index, obtained from the GT simulations. The average CPCP is annotated at the bottom right of each panel. As the Kp index increases from 1 to 5, the convection pattern becomes more complex and the corresponding CPCP increases from 19 to 101 kV. This result is consistent with the convection patterns from the Weimer 05 empirical model, as depicted in Figure 12b. However, the CPCP in the empirical model increases from 40 to 84 kV as the Kp index increases from 1 to 5, suggesting that the global simulation may overestimate the ionospheric potential for active conditions. Moreover, the negative potential cells are smaller than the positive cells in the GT simulation when Kp is larger than 1, which is the opposite in the empirical model.
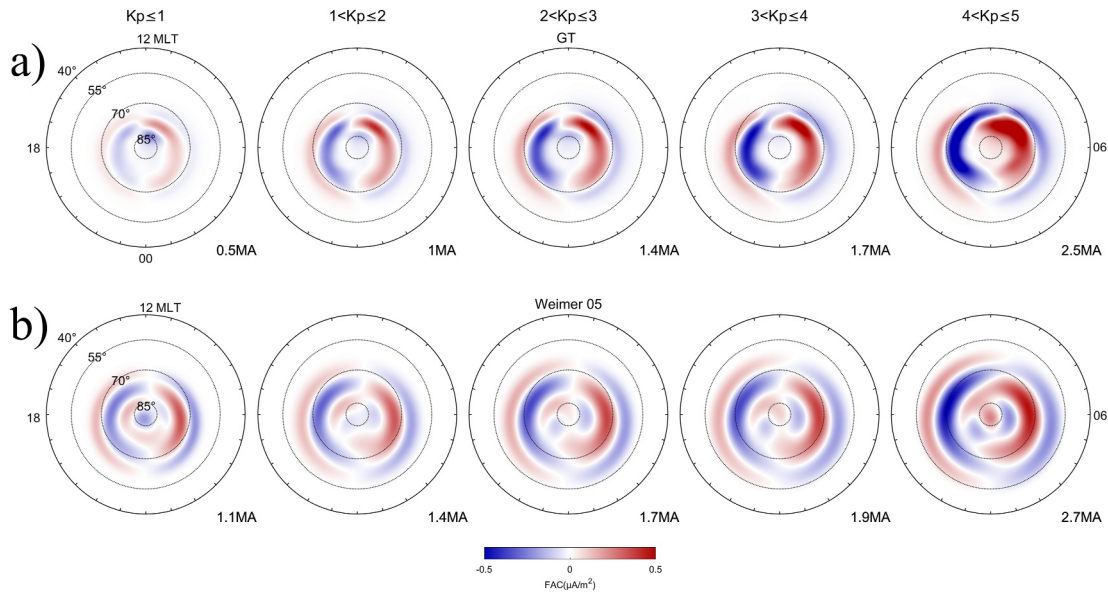
Figure 11. Statistical distributions of ionospheric FAC depending on Kp index, obtained from (a) the GT simulation and (b) Weimer 05 empirical models under the same conditions as the GT simulation.

Figure 13a displays the average distributions of Joule heating in the GT simulation, which are classified by the Kp index. The magnitude of hemispheric Joule heating increases from 10 to 146 GW. In the Weimer 05 empirical model (Figure 13b), the hemispheric Joule heating increases from 16 to 103 GW, which is lower than the simulation results. The discrepancy in the hemispheric Joule heating power is possibly due to the electric potential being smaller in the empirical model. However, the main difference is the GT model simulates the enhancement in the polar cusp region, which is not evident in the empirical model. The total Joule heating of both models increases with the increasing Kp index, but the empirical model produces a smaller value than the GT simulation for Kp > 3, and a larger value for Kp ≤ 2.
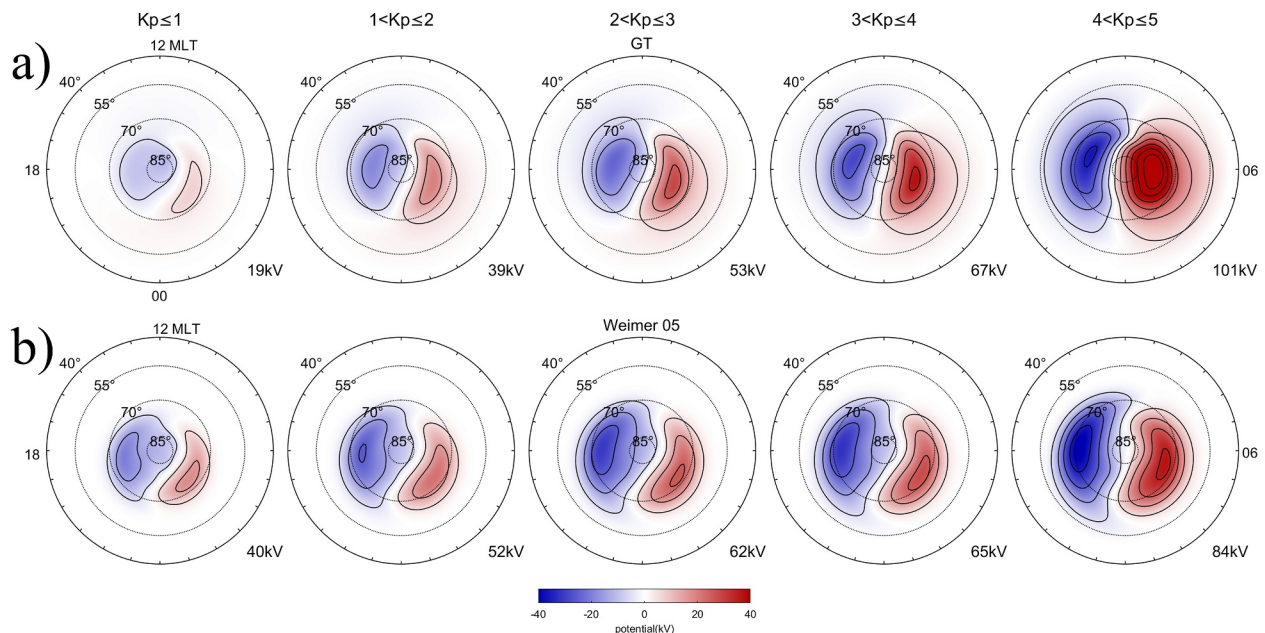

Figure 12. Statistical convection patterns depending on the Kp index, obtained from (a) the GT simulation and (b) Weimer 05 empirical models under the same conditions as the GT simulation.
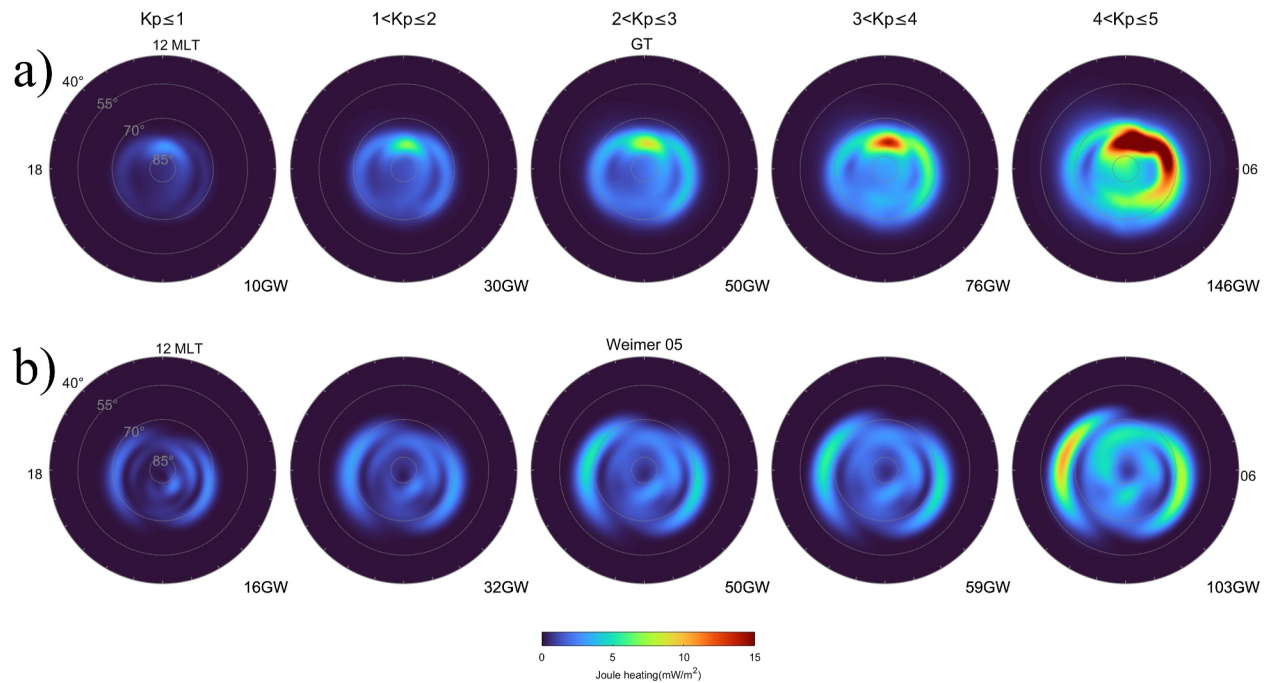
Figure 13. Statistical Joule heating distribution depending on Kp index, obtained from (a) the GT simulation and (b) Weimer 05 empirical models under the same as GT simulation conditions.

Figure 14 presents the Kp-dependence of the average downward Alfvénic Poynting flux, obtained from the GT simulations. As the Kp index increases, the Alfvénic power also increases, ranging from 0.3 to 2.6 GW, indicating a more pronounced pattern. This increase is consistent with the fact that during high Kp index periods, the magnetosphere becomes more active, resulting in enhanced Alfvén wave activities. Conversely, when Kp is less than 1, the Alfvénic Poynting flux is not prominent, and the hemispheric integrated Alfvénic power is only 0.3 GW. For $3 < Kp \leq 4$, the average Poynting flux is less intense than the results from the 24-hr LFM run under the mean Kp = 3 condition (Zhang et al., 2012), but it is similar to the Polar one-year average values under mean Kp = 2 condition, as reported by Keiling et al. (2003). When the Kp index is larger than 2, the distributions of average Alfvénic Poynting flux exhibit significant dawn-dusk asymmetry, with the pre-midnight flux being enhanced and the peak occurring near 75° MLAT. This is consistent with the statistical distribution of median peak values of dispersive Alfvén-wave Poynting fluxes derived from low-altitude FAST measurements, which peak near 73° MLAT (Chaston et al., 2003). Moreover, this distribution is also consistent with the statistical distribution of the energy flux of "broadband" electron precipitation observed in DMSP particle precipitation data set. For high solar wind driving conditions, this distribution exhibits a broad pre-midnight peak between 71° and
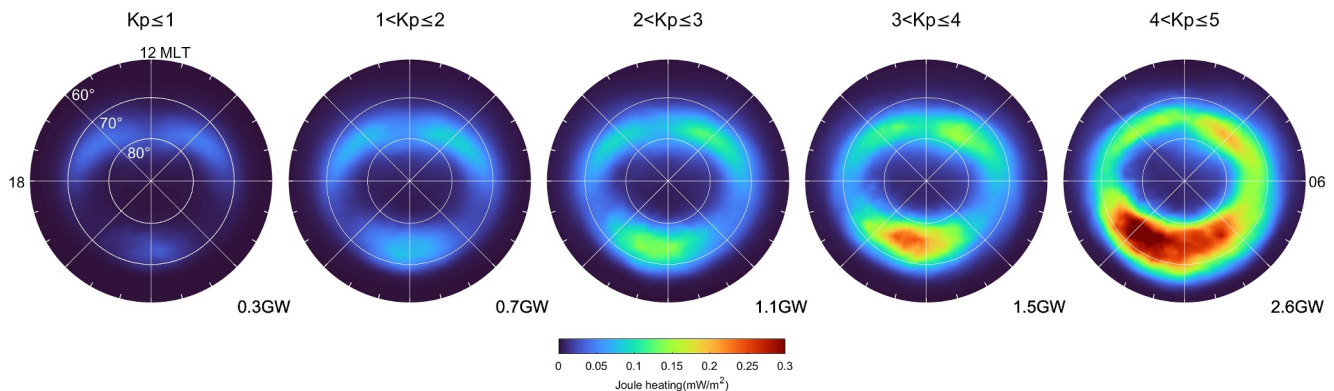

Figure 14. Statistical ionospheric Alfvénic Poynting flux distribution depending on Kp index, obtained from the GT simulation.
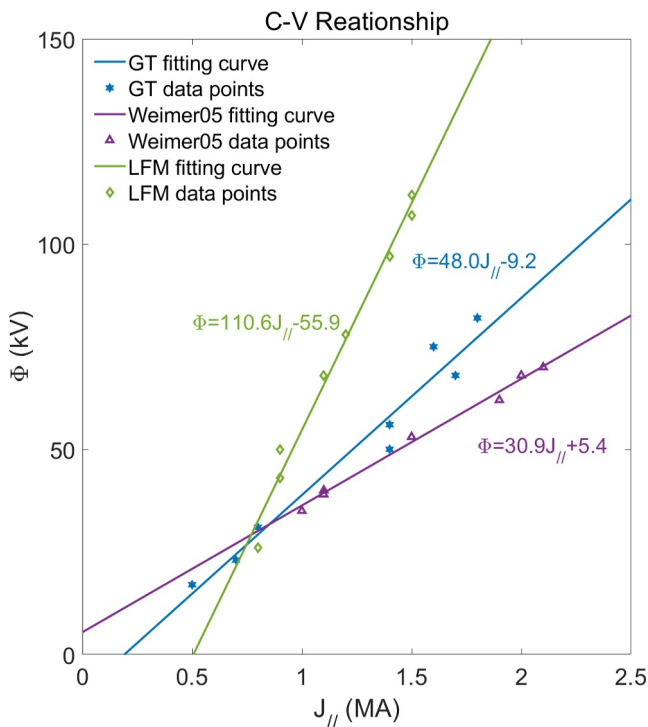
Figure 15. Current-voltage relationship for GT, LFM and Weimer 05 empirical model.

77° MLAT (Newell et al., 2009), and broadband electron precipitation MLT-MLAT distribution may be considered as a proxy for Alfvén wave energy flux (Chaston et al., 2003).

3.3. The Relationship Between the Current and Potential

Using the hemispheric downward current and CPCP values in each clock angle bin, the current-voltage relation is derived from both the GT simulations and the Weimer 05 empirical model results. Figure 15 shows the average current-voltage relation derived from the GT simulations, together with the results from LFM simulations used in Zhang et al. (2011). The empirical current-voltage relation from Weimer 05 is also shown in Figure 15 as a reference. The linear equation of each fitted curve is shown on the graph in the same color as the data points. The slopes calculated from the LFM and the GT simulation are 110.6 and 48.0 kV/MA, respectively, both of which are higher than the value of 30.9 kV/MA derived from the empirical model. It is evident that using the empirical slope as a baseline, the current-voltage relation in the GT simulation is improved significantly compared to the LFM simulation used in Zhang et al. (2011). Although, the LFM code has been a well-known global terrestrial magnetosphere model, widely used in geospace research and space weather applications.

The GAMERA code in the GT simulation extends the capabilities of the LFM and provides significant improvements. In the LFM model, the inner boundary processing exhibits significant noise. However, GAMERA has implemented an upgraded algorithm and improved the treatment of boundary conditions, resulting in a solution without the issues encountered in the LFM. Therefore, the solution obtained from GT yields more reasonable results compared to LFM. it should be acknowledged that various factors, including the grid configuration, may contribute to the simulated outcomes. Thus, the specific impact warrants further investigation through quantitative comparison simulations in the future.

4. Summary

This study focuses on the statistical features of M-I coupling using the GT configuration of the MAGE model which couples the M-I system. The M-I coupling characteristics, including field-aligned current, polar cap potential, ionospheric Joule heating, and the downward Alfvénic Poynting flux, were binned according to IMF clock angles and Kp index over an entire Carrington Rotation event. The main conclusions are given as follows.

1. The average distributions of FAC, binned on the IMF clock angle in the GT simulation, agree with observations from Iridium, the Weimer 05 empirical model, and the AMPS empirical model. The magnitude of the average FAC in the simulation is more closely to Iridium observations. The GT simulation reproduces the typical R1 and R2 pattern for the FAC systems and the R0 current system for "Northward B_z" without obvious artificial structure caused by numerical dissipation in the polar regions.
2. The convection patterns classified by IMF clock angle are consistent with those of both the SuperDARN measurements and the Weimer 05 empirical model, displaying the typical dual dawn-dusk asymmetrical cell pattern. The values of CPCP are higher in the GT simulation due to the SuperDARN data sets covering different periods with simulation.
3. The Joule heating is primarily distributed in the area between R1 and R2 current systems, indicating that the R1 currents are close to the R2 currents at lower latitudes (around 70° MLAT) in the GT simulation, The GT simulation also reveals the pronounced Joule heating around the cusp region, which is also reported in Cosgrove's empirical model and observations. The downward DC Poynting flux in the LFM simulation is much more prominent in the high latitude polar region (inside 75° MLAT) than in the GT simulation, indicating that the MAGE model has been greatly improved as compared to the LFM model.

4. The distribution of average downward Alfvénic Poynting flux shows a noticeable dawn-dusk asymmetry under the southward IMF clock angle, which is evident for observations by Polar satellite. The signatures are also consistent with the IAW Poynting flux observed by FAST.
5. In addition, the distribution of Joule heating and its correlation with FAC and CPCP indicates that the GT simulation outperforms the Weimer 05 empirical model in terms of statistical analysis based on the Kp index. Furthermore, observations demonstrate that the GT simulation is able to accurately replicate the M-I coupling process as reflected in the distribution of Alfvénic Poynting flux depending on the Kp index during the quiet period (Kp $\leq$ 5).
6. The analysis of the Current-voltage relationship proposes that the GT simulation agrees with the Weimer 05 empirical model better than the LFM global MHD model, illustrating that the new global simulation is significantly improved and can demonstrate the statistical features of M-I coupling well.

Overall, the global geospace simulations have shown great promise in characterizing and quantifying M-I coupling behavior, enabling the scientific community to improve space weather forecasting and further our knowledge of the complex interactions between the Earth's magnetosphere and ionosphere-thermosphere system. Our M-I coupled model demonstrates improved accuracy in reproducing several physical structures, such as the well-defined FAC boundary, the typical asymmetric "crescent-round" pattern, and the cusp Joule heating enhancement, compared to the LFM model. Future research will further analyze the influence of the specific internal relationship of the improved model itself on M-I coupling and give more detailed quantitative results, such as the influence of grid resolution, upwind reconstruction order, etc.

Data Availability Statement

The model outputs used to generate the figures for analysis presented in this paper and some related input documents for the GT simulation are being preserved online (Yin, 2024).

References

Anderson, B. J., Korth, H., Waters, C. L., Green, D. L., & Stauning, P. (2008). Statistical Birkeland current distributions from magnetic field observations by the Iridium constellation. *Annales Geophysicae*, 26(3), 671–687. https://doi.org/10.5194/angeo-26-671-2008

Bhattarai, S. K., Lopez, R. E., Bruntz, R., Lyon, J. G., & Wiltberger, M. (2012). Simulation of the polar cap potential during periods with northward interplanetary magnetic field. *Journal of Geophysical Research*, 117(A4), A04219. https://doi.org/10.1029/2011JA017143

Billett, D. D., Perry, G. W., Clausen, L. B. N., Archer, W. E., McWilliams, K. A., Haaland, S., et al. (2021). The relationship between large scale thermospheric density enhancements and the spatial distribution of Poynting flux. *Journal of Geophysical Research: Space Physics*, 126(5), e2021JA029205. https://doi.org/10.1029/2021ja029205

Bjoland, L. M., Chen, X., Jin, Y., Reimer, A. S., Skjaeveland, Å., Wessel, M. R., et al. (2015). Interplanetary magnetic field and solar cycle dependence of Northern Hemisphere F region joule heating. *Journal of Geophysical Research: Space Physics*, 120(2), 1478–1487. https://doi.org/10.1002/2014ja020586

Bruntz, R., Lopez, R. E., Bhattarai, S. K., Pham, K. H., Deng, Y., Huang, Y., et al. (2012). Investigating the viscous interaction and its role in generating the ionospheric potential during the whole heliosphere interval. *Journal of Atmospheric and Solar-Terrestrial Physics*, 83, 70–78. https://doi.org/10.1016/j.jastp.2012.03.016

Chaston, C., Bonnell, J., Carlson, C., McFadden, J., Ergun, R., & Strangeway, R. (2003). Properties of small-scale Alfvén waves and accelerated electrons from FAST. *Journal of Geophysical Research*, 108(A4), 8003. https://doi.org/10.1029/2002JA009420

Codrescu, M. V., Fuller-Rowell, T. J., & Foster, J. C. (1995). On the importance of E-field variability for Joule heating in the high-latitude thermosphere. *Geophysical Research Letters*, 22(17), 2393–2396. https://doi.org/10.1029/95GL01909

Codrescu, M. V., Negrea, C., Fedrizzi, M., Fuller-Rowell, T. J., Dobin, A., Jakowsky, N., et al. (2012). A real-time run of the Coupled Thermosphere Ionosphere Plasmasphere Electrodynamics (CTIPe) model. *Space Weather*, 10(2), S02001. https://doi.org/10.1029/2011sw000736

Cosgrove, R. B., Bahcivan, H., Chen, S., Strangeway, R. J., Ortega, J., Alhassan, M., et al. (2014). Empirical model of Poynting flux derived from FAST data and a cusp signature. *Journal of Geophysical Research: Space Physics*, 119(1), 411–430. https://doi.org/10.1002/2013JA019105

Dang, T., Zhang, B., Lei, J., Wang, W., Burns, A., Liu, H.-L., et al. (2021). Azimuthal averaging–reconstruction filtering techniques for finite-difference general circulation models in spherical geometry. *Geoscientific Model Development*, 14(2), 859–873. https://doi.org/10.5194/gmd-14-859-2021

Goertz, C. K., & Boswell, R. W. (1979). Magnetosphere-ionosphere coupling. *Journal of Geophysical Research*, 84(A12), 7239–7246. https://doi.org/10.1029/ja084ia12p07239

Guild, T. B., Spence, H. E., Kepko, E. L., Merkin, V., Lyon, J. G., Wiltberger, M., & Goodrich, C. C. (2008a). Geotail and LFM comparisons of plasma sheet climatology: 1. Average values. *Journal of Geophysical Research*, 113(A4), A04216. https://doi.org/10.1029/2007ja012611

Guild, T. B., Spence, H. E., Kepko, E. L., Merkin, V., Lyon, J. G., Wiltberger, M., & Goodrich, C. C. (2008b). Geotail and LFM comparisons of plasma sheet climatology: 2. Flow variability. *Journal of Geophysical Research*, 113(A4), A04217. https://doi.org/10.1029/2007ja012613

Hagan, M. E., & Forbes, J. M. (2002). Migrating and nonmigrating diurnal tides in the middle and upper atmosphere excited by tropospheric latent heat release. *Journal of Geophysical Research*, 107(D24), 4754. https://doi.org/10.1029/2001JD001236

Hagan, M. E., & Forbes, J. M. (2003). Migrating and nonmigrating semidiurnal tides in the upper atmosphere excited by tropospheric latent heat release. *Journal of Geophysical Research*, 108(A2), 1062. https://doi.org/10.1029/2002JA009466

Hatch, S. M., LaBelle, J., Lotko, W., Chaston, C. C., & Zhang, B. (2017). IMF control of Alfvénic energy transport and deposition at high latitudes. *Journal of Geophysical Research: Space Physics*, 122(12), 12189–12211. https://doi.org/10.1002/2017JA024175

Huang, C.-L., Spence, H. E., Lyon, J. G., Toffoletto, F. R., Singer, H. J., & Sazykin, S. (2006). Storm-time configuration of the inner magnetosphere: Lyon-Fedder-Mobarry MHD code, Tsyganenko model, and GOES observations. *Journal of Geophysical Research*, *111*(A11), A11S16. https://doi.org/10.1029/2006ja011626

Iijima, T., & Potemra, T. A. (1976). The amplitude distribution of field-aligned currents at northern high latitudes observed by Triad. *Journal of Geophysical Research*, *81*(13), 2165–2174. https://doi.org/10.1029/JA081i013p02165

Iijima, T., & Potemra, T. A. (1978). Large-scale characteristics of field-aligned currents associated with substorms. *Journal of Geophysical Research*, *83*(A2), 599–615. https://doi.org/10.1029/JA083iA02p00599

Iijima, T., Potemra, T. A., Zanetti, L. J., & Bythrow, P. F. (1984). Large-scale Birkeland currents in the dayside polar region during strongly northward IMF: A new Birkeland current system. *Journal of Geophysical Research*, *89*(A9), 7441–7452. https://doi.org/10.1029/ja089ia09p07441

Keiling, A., Thaller, S., Dombeck, J., & Wygant, J. (2020). Temporal evolution of substorm-driven global Alfvén wave power above the auroral acceleration region. *Journal of Geophysical Research: Space Physics*, *125*(4), e2019JA027444. https://doi.org/10.1029/2019ja027444

Keiling, A., Thaller, S., Wygant, J., & Dombeck, J. (2019). Assessing the global Alfven wave power flow into and out of the auroral acceleration region during geomagnetic storms. *Science Advances*, *5*(6), eaav8411. https://doi.org/10.1126/sciadv.aav8411

Keiling, A., Wygant, J. R., Cattell, C. A., Mozer, F. S., & Russell, C. T. (2003). The global morphology of wave Poynting flux: Powering the aurora. *Science*, *299*(5605), 383–386. https://doi.org/10.1126/science.1080073

Laundal, K. M., Finlay, C. C., Olsen, N., & Reistad, J. P. (2018). Solar wind and seasonal influence on ionospheric currents from swarm and CHAMP measurements. *Journal of Geophysical Research: Space Physics*, *123*(5), 4402–4429. https://doi.org/10.1029/2018ja025387

Li, W., Knipp, D., Lei, J., & Raeder, J. (2011). The relation between dayside local Poynting flux enhancement and cusp reconnection. *Journal of Geophysical Research*, *116*(A8), A08301. https://doi.org/10.1029/2011ja016566

Lin, D., Sorathia, K., Wang, W., Merkin, V., Bao, S., Pham, K., et al. (2021). The role of diffuse electron precipitation in the formation of subauroral polarization streams. *Journal of Geophysical Research: Space Physics*, *126*(12), e2021JA029792. https://doi.org/10.1029/2021ja029792

Lotko, W., Smith, R. H., Zhang, B., Ouellette, J. E., Brambles, O. J., & Lyon, J. G. (2014). Ionospheric control of magnetotail reconnection. *Science*, *345*(6193), 184–187. https://doi.org/10.1126/science.1252907

Lyon, J. G., Fedder, J. A., & Mobarry, C. M. (2004). The Lyon–Fedder–Mobarry (LFM) global MHD magnetospheric simulation code. *Journal of Atmospheric and Solar-Terrestrial Physics*, *66*(15–16), 1333–1350. https://doi.org/10.1016/j.jastp.2004.03.020

Matzka, J., Stolle, C., Yamazaki, Y., Bronkalla, O., & Morschhauser, A. (2021). The geomagnetic Kp index and derived indices of geomagnetic activity. *Space Weather*, *19*(5), e2020SW002641. https://doi.org/10.1029/2020SW002641

Merkin, V. G., & Lyon, J. G. (2010). Effects of the low-latitude ionospheric boundary condition on the global magnetosphere. *Journal of Geophysical Research*, *115*(A10), A10202. https://doi.org/10.1029/2010ja015461

Newell, P. T., Sotirelis, T., & Wing, S. (2009). Diffuse, monoenergetic, and broadband aurora: The global precipitation budget. *Journal of Geophysical Research*, *114*(A9), A09207. https://doi.org/10.1029/2009JA014326

Pettigrew, E., Shepherd, S., & Ruohoniemi, J. (2010). Climatological patterns of high-latitude convection in the Northern and Southern hemispheres: Dipole tilt dependencies and interhemispheric comparisons. *Journal of Geophysical Research*, *115*(A7), A07305. https://doi.org/10.1029/2009JA014956

Pham, K. H., Zhang, B., Sorathia, K., Dang, T., Wang, W., Merkin, V., et al. (2022). Thermospheric density perturbations produced by traveling atmospheric disturbances during August 2005 storm. *Journal of Geophysical Research: Space Physics*, *127*(2), e2021JA030071. https://doi.org/10.1029/2021ja030071

Raeder, J., Larson, D., Li, W., Kepko, E. L., & Fuller-rowell, T. (2008). OpenGGCM simulations for the THEMIS mission. *Space Science Reviews*, *141*(1–4), 535–555. https://doi.org/10.1007/s11214-008-9421-5

Richmond, A. D., Ridley, E. C., & Roble, R. G. (1992). A thermosphere/ionosphere general circulation model with coupled electrodynamics. *Geophysical Research Letters*, *19*(6), 601–604. https://doi.org/10.1029/92GL00401

Roble, R. G., Ridley, E. C., Richmond, A. D., & Dickinson, R. E. (1988). A coupled thermosphere/ionosphere general circulation model. *Geophysical Research Letters*, *15*(12), 1325–1328. https://doi.org/10.1029/GL015i012p01325

Sorathia, K. A., Merkin, V. G., Panov, E. V., Zhang, B., Lyon, J. G., Garretson, J., et al. (2020). Ballooning-interchange instability in the near-Earth plasma sheet and auroral beads: Global magnetospheric modeling at the limit of the MHD approximation. *Geophysical Research Letters*, *47*(14), e2020GL088227. https://doi.org/10.1029/2020gl088227

Tenfjord, P., Østgaard, N., Snekvik, K., Laundal, K. M., Reistad, J. P., Haaland, S., & Milan, S. E. (2015). How the IMF By induces a By component in the closed magnetosphere and how it leads to asymmetric currents and convection patterns in the two hemispheres. *Journal of Geophysical Research: Space Physics*, *120*(11), 9368–9384. https://doi.org/10.1002/2015ja021579

Toffoletto, F. R., Sazykin, S., Spiro, R. W., & Wolf, R. A. (2003). Inner magnetosphere modeling with the rice convection model. *Space Science Reviews*, *107*(1/2), 175–196. https://doi.org/10.1023/A:1025532008047

Tóth, G., Sokolov, I. V., Gombosi, T. I., Chesney, D. R., Clauer, C. R., De Zeeuw, D. L., et al. (2005). Space weather modeling framework: A new tool for the space science community. *Journal of Geophysical Research*, *110*(A12), A12226. https://doi.org/10.1029/2005JA011126

Tóth, G., Van Der Holst, B., Sokolov, I. V., De Zeeuw, D. L., Gombosi, T. I., Fang, F., et al. (2012). Adaptive numerical algorithms in space weather modeling. *Journal of Computational Physics*, *231*(3), 870–903. https://doi.org/10.1016/j.jcp.2011.02.006

Wang, W., Wiltberger, M., Burns, A., Solomon, S., Killeen, T., Maruyama, N., & Lyon, J. (2004). Initial results from the coupled magnetosphere–ionosphere–thermosphere model: Thermosphere–ionosphere responses. *Journal of Atmospheric and Solar-Terrestrial Physics*, *66*(15–16), 1425–1441. https://doi.org/10.1016/j.jastp.2004.04.008

Wang, X., Miao, J., Aa, E., Ren, T., Wang, Y., Liu, J., & Liu, S. (2020). Statistical analysis of joule heating and thermosphere response during geomagnetic storms of different magnitudes. *Journal of Geophysical Research: Space Physics*, *125*(8), e2020JA027966. https://doi.org/10.1029/2020ja027966

Weimer, D. R. (2005). Improved ionospheric electrodynamic models and application to calculating Joule heating rates. *Journal of Geophysical Research*, *110*(A5), A05306. https://doi.org/10.1029/2004JA010884

Wiltberger, M., Rigler, E., Merkin, V., & Lyon, J. (2017). Structure of high latitude currents in magnetosphere-ionosphere models. *Space Science Reviews*, *206*(1–4), 575–598. https://doi.org/10.1007/s11214-016-0271-2

Wiltberger, M., Wang, W., Burns, A., Solomon, S., Lyon, J., & Goodrich, C. (2004). Initial results from the coupled magnetosphere ionosphere thermosphere model: Magnetospheric and ionospheric responses. *Journal of Atmospheric and Solar-Terrestrial Physics*, *66*(15–16), 1411–1423. https://doi.org/10.1016/j.jastp.2004.03.026

Wiltberger, M., Weigel, R. S., Lotko, W., & Fedder, J. A. (2009). Modeling seasonal variations of auroral particle precipitation in a global-scale magnetosphere-ionosphere simulation. *Journal of Geophysical Research*, *114*(A1), A01204. https://doi.org/10.1029/2008ja013108

Yin, Q. (2024). Validation of simulated statistical characteristics of magnetosphere-ionosphere coupling. In *Global geospace simulations over an entire Carrington rotation*. https://doi.org/10.17605/OSF.IO/BPZKF

Zhang, B., Brambles, O. J., Cassak, P. A., Ouellette, J. E., Wiltberger, M., Lotko, W., & Lyon, J. G. (2017). Transition from global to local control of dayside reconnection from ionospheric-sourced mass loading. *Journal of Geophysical Research: Space Physics*, *122*(9), 9474–9488. https://doi.org/10.1002/2016ja023646

Zhang, B., Lotko, W., Brambles, O., Damiano, P., Wiltberger, M., & Lyon, J. (2012). Magnetotail origins of auroral Alfvenic power. *Journal of Geophysical Research*, *117*(A9), A09205. https://doi.org/10.1029/2012ja017680

Zhang, B., Lotko, W., Brambles, O., Wiltberger, M., & Lyon, J. (2015). Electron precipitation models in global magnetosphere simulations. *Journal of Geophysical Research: Space Physics*, *120*(2), 1035–1056. https://doi.org/10.1002/2014ja020615

Zhang, B., Lotko, W., Brambles, O., Xi, S., Wiltberger, M., & Lyon, J. (2014). Solar wind control of auroral Alfvénic power generated in the magnetotail. *Journal of Geophysical Research: Space Physics*, *119*(3), 1734–1748. https://doi.org/10.1002/2013ja019178

Zhang, B., Lotko, W., Wiltberger, M., Brambles, O., & Damiano, P. (2011). A statistical study of magnetosphere–ionosphere coupling in the Lyon–Fedder–Mobarry global MHD model. *Journal of Atmospheric and Solar-Terrestrial Physics*, *73*(5–6), 686–702. https://doi.org/10.1016/j.jastp.2010.09.027

Zhang, B., Sorathia, K. A., Lyon, J. G., Merkin, V. G., Garretson, J. S., & Wiltberger, M. (2019). Gamera: A three-dimensional finite-volume MHD solver for non-orthogonal curvilinear geometries. *The Astrophysical Journal - Supplement Series*, *244*(1), 20. https://doi.org/10.3847/1538-4365/ab3a4c